



# Electron firehose instability: Kinetic linear theory and two-dimensional particle-in-cell simulations

Enrico Camporeale<sup>1</sup> and David Burgess<sup>1</sup>

Received 18 January 2008; revised 28 March 2008; accepted 24 April 2008; published 29 July 2008.

[1] The kinetic electron firehose instability (EFI) is thought to be a crucial mechanism for constraining the observed electron anisotropy in expanding astrophysical plasmas, such as the solar wind. The EFI arises in a bi-Maxwellian plasma when the parallel temperature is greater than the perpendicular one, and its effect is to reduce anisotropy. We study this mechanism via kinetic linear theory, extending and refining previous results, and by new two-dimensional particle-in-cell (PIC) simulations with physical mass ratio. The results of PIC simulations show under which conditions the EFI can indeed be regarded as a constraint for electron distribution function. The detailed electron physics near marginal stability condition is discussed, with emphasis on the competition between growing and damping modes and on wave patterns formed at the nonlinear stage. The results also suggest an observational signature that the EFI has operated, namely the appearance of low-frequency, quasisperpendicular whistler/electron–cyclotron waves.

**Citation:** Camporeale, E., and D. Burgess (2008), Electron firehose instability: Kinetic linear theory and two-dimensional particle-in-cell simulations, *J. Geophys. Res.*, *113*, A07107, doi:10.1029/2008JA013043.

## 1. Introduction

[2] Recent spacecraft observations of protons and electrons in the solar wind have shown that the temperature anisotropy developed by both species does not agree with an adiabatic expansion of the wind. The scenario invoked by some authors to justify the low level of anisotropy observed is that linear instabilities such as the whistler and mirror (for  $T_{\perp}/T_{\parallel} > 1$ ) and the firehose (for  $T_{\perp}/T_{\parallel} < 1$ ) play the role of constraints to the development of larger temperature anisotropies. This would be in accord with the long-standing idea that any linear instability acts in such a way as to reduce the source of free energy, i.e., the initial driver of the instability, which in this case is the temperature anisotropy. The idea of a linear instability threshold as a constraint for the development of temperature anisotropy has been investigated through observations, linear theory and computer simulations, for electrons [Gary *et al.*, 2000; Messmer, 2002; Gary and Nishimura, 2003; Gary *et al.*, 2005; Stverak *et al.*, 2008] and protons [Quest and Shapiro, 1996; Kasper *et al.*, 2002; Hellinger *et al.*, 2006; Matteini *et al.*, 2006, 2007], and for both cases:  $T_{\perp}/T_{\parallel} < 1$  and  $T_{\perp}/T_{\parallel} > 1$ .

[3] The unifying method of research for all these works is to seek a threshold condition for the anisotropy of the form

$$\frac{T_{\perp}}{T_{\parallel}} = 1 + \frac{S}{\beta_{\parallel}^{\alpha}} \quad (1)$$

where the parallel and perpendicular directions are with respect to the background magnetic field,  $\beta_{\parallel} = 8\pi n_j k_B T_{\parallel j} /$

$B_0^2$ ,  $S$  and  $\alpha$  are constants, and all other symbols are conventional. It is assumed that for appropriate values of  $S$  and  $\alpha$ , equation (1) represents a good approximation for a curve with constant linear growth rate in the  $(T_{\perp}/T_{\parallel}, \beta_{\parallel})$  parameter space. In other words, to adopt equation (1) as a threshold is equivalent to stating that the anisotropy is constrained by a certain *ad hoc* value of the linear growth rate. Observational studies confirm that this argument is successful, and indeed in some cases statistical evidence has been reported for distributions with a level of anisotropy constrained within a certain value of the linear growth rate [see e.g. Gary *et al.*, 2005; Hellinger *et al.*, 2006; Matteini *et al.*, 2007].

[4] In this paper we focus on the electron firehose instability (EFI), which is driven by a parallel electron temperature greater than the perpendicular one. In a fluid picture the anisotropy  $T_{\parallel} > T_{\perp}$  is caused by the expansion of the solar wind. For instance in the CGL approximation [Chew *et al.*, 1956], assuming a radially expanding plasma, the ratio  $T_{\parallel}/T_{\perp}$  is predicted to increase proportionally to the square of the distance from the Sun. Observations show a completely different behavior and the Firehose Instability therefore is expected to play a crucial role in this scenario.

[5] The linear theory for the EFI has been presented recently by Li and Habbal [2000], and one-dimensional particle-in-cell (PIC) simulation results (for nonphysical mass ratio  $m_i/m_e$ ) have been obtained by Messmer [2002] (for parallel propagation) and by Gary *et al.* [2005] (for oblique propagation). Furthermore, a study of the EFI by means of test particle simulations has been conducted by Paesold and Benz [2003].

[6] The purpose of the present paper is to refine these results showing PIC simulations for a two-dimensional geometry and for physical mass ratio. There are at least

<sup>1</sup>Astronomy Unit, Queen Mary University of London, London, UK.

three reasons why such study is of great importance in the previously outlined framework. First, although it is well known that the EFI is dominated by highly oblique perturbations for every value of  $\beta_{\parallel e}$ , it cannot be excluded that in a nonlinear stage after the saturation of the linear instability, quasiparallel waves are excited. The shift toward smaller angles of propagation and longer wavelengths is in some sense already evident, as we will show, within the linear theory but it has to be quantified with a nonlinear study, such as with a PIC simulation. Second, previous simulations conducted with a one-dimensional slab geometry oriented along the most rapidly growing perturbation, showed that the final states of the instability were aligned on a contour of constant linear growth rate, described in equation (1), even if started from different initial conditions (see Figure 5 in Gary *et al.* [2005]). This has been confuted by observations that reported the existence of electrons within a certain finite range of  $\beta_{\parallel e}$  and  $T_{\perp}/T_{\parallel}$  near the marginal stability, and not aligned on a single curve [Stverak *et al.*, 2008].

[7] Third, two-dimensional simulations offer a computational and theoretical background to the observational community, highlighting signatures of particular waves associated with the instability development, that could be a valuable insight for future data analysis.

[8] Therefore there is a clear need for a two-dimensional simulation in order to study not only the particle–wave interactions that scatter the particles and reduce the anisotropy, but also to study the interactions among waves propagating at different angles, and to look at the final distribution of wave patterns in space. The idea behind the PIC simulations presented in this paper is to study the evolution of the plasma starting from an unstable state with relatively high linear growth rate, and to follow it toward marginal stability. Therefore we do not focus on the mechanism leading the system to such an unstable condition, but we assume it as our starting point.

[9] The paper is organized as follows. In section 2 we review the linear Vlasov theory for the EFI, presenting new plots and focusing on the competition between propagating and nonpropagating modes. In section 3 we present and discuss the results of our simulations. Finally, in section 4 we draw our conclusions.

## 2. Linear Vlasov Theory

[10] The linear properties of the kinetic EFI have been elucidated by Li and Habbal [2000], Paesold and Benz [1999], and Gary and Madland [1985], among others. In this section we confirm and extend those results. We study a collisionless bi-Maxwellian plasma of electrons and protons within an uniform background magnetic field  $\mathbf{B}_0$ . The normal modes of the linearized Vlasov equation are found with the well-established technique for a homogeneous bi-Maxwellian plasma, where it is assumed that the initial equilibrium distribution function  $f_0(\mathbf{x}, \mathbf{v}, \mathbf{t})$  is disturbed with a small linear perturbation of the form  $f_1 \exp[i(\mathbf{k} \cdot \mathbf{x} - \omega t)]$ , where in general  $f_1$  is a complex amplitude [e.g., Stix, 1992].

[11] The common procedure boils down to rewriting the linear problem as

$$D(\mathbf{k}, \omega) \cdot \mathbf{E} = 0, \quad (2)$$

where  $D$  is a  $3 \times 3$  complex matrix, whose elements are functions of  $\mathbf{k}$ ,  $\omega$ , and the equilibrium thermal velocities in the parallel and perpendicular directions, and  $\mathbf{E}$  is the perturbed electric field. The dispersion relation  $\omega = \omega(\mathbf{k})$  is found by solving for the determinant of  $D$  to be null, that is the condition for equation (2) to yield a nontrivial solution. The complex eigenvalues of the problem  $\omega = \omega_r + i\gamma$  are found through the numerical solution of  $|D| = 0$ , by means of a root-finding algorithm.

[12] We choose the same plasma parameters adopted by Li and Habbal [2000], to facilitate comparisons. The ratio of Alfvén speed to speed of light,  $v_A/c$ , is set equal to  $10^{-3}$ , and the plasma  $\beta = 8\pi n k_B T / |B_0|^2$  (where  $n$  is the plasma density,  $k_B$  is the Boltzmann constant,  $T$  is temperature) is equal to 1 for protons. The range of  $\beta_{\parallel e}$  studied varies from 2.5 to 10, for all angles of propagation  $\theta$  ( $\cos \theta = \mathbf{k} \cdot \mathbf{B}_0 / |\mathbf{k}| |\mathbf{B}_0|$ ), and  $T_{\perp e} / T_{\parallel e}$  varies from 0.9 to 0.1 (we will omit the subscript  $e$ , referring always to the electron temperature). The proton distribution is Maxwellian.

[13] It is known that the EFI presents two branches: one with  $\omega_r = 0$ , and the other with  $\omega_r \neq 0$ . Unfortunately no unique nomenclature has been established yet. Li and Habbal [2000] termed “quasiparallel” and “oblique” perturbations with respectively  $\omega_r = 0$  and  $\theta < 30^\circ$ , and  $\omega_r > 0$  and  $\theta > 30^\circ$  (see their Table [1]), while Gary and Nishimura [2003] referred to the electron resonance factor as a distinguishing feature, and dubbed the parallel wave “nonresonant”, and the oblique wave “resonant”. As we will show the propagating nonresonant perturbations extend to quasiperpendicular angle ( $\theta > 50^\circ$ ), thus making both choices of nomenclature ambiguous. We will henceforth refer to the different branches according only to their propagating ( $\omega_r \neq 0$ ) or nonpropagating ( $\omega_r = 0$ ) nature, irrespective of the angle  $\theta$ . It is worth mentioning however, that in agreement with Li and Habbal [2000] we have not found any nonpropagating perturbation in the parallel direction (and for small angles). It is also generally true that the nonpropagating branch has a larger growth rate than the propagating one.

[14] We now comment on the main properties of the  $\omega_r = 0$  branch.

[15] In Figure 1 we show the contour plots of the maximum growth rate  $\gamma_m / \Omega_e$  as a function of the angle  $\theta$  and of the anisotropy ( $1 - T_{\perp} / T_{\parallel}$ ), for four different values of  $\beta_{\parallel e} = 10, 7.5, 5, 2.5$ . The contours tend to become vertical at low  $\theta$ , and horizontal at high  $\theta$ , meaning that the growth rate is highly dependent on the level of anisotropy for large  $\theta$  and almost independent for small  $\theta$ . Also in each plot the value of  $\theta_m$  (the angle for which  $\gamma$  reaches its maximum at fixed anisotropy) decreases as the anisotropy decreases. For  $\beta_{\parallel e} = 2.5$ , the instability is confined above the value of anisotropy  $(1 - T_{\perp} / T_{\parallel}) > 0.6$ , but the range of angles involved is broader, with a nonvanishing  $\gamma$  for  $\theta < 50^\circ$ .

[16] In Figure 2 we show the values of  $\gamma_m / \Omega_e$  (top) and  $\theta_m$  (bottom) as functions of  $T_{\perp} / T_{\parallel}$ . The four curves are again for four values of  $\beta_{\parallel e} = 10, 7.5, 5, 2.5$ , with the arrows indicating the increasing direction. This plot might be compared with Figure 5 of Li and Habbal [2000]. In the bottom plot it is again clear that  $\theta_m$  decreases as the anisotropy decreases. Furthermore what emerges is that as the factor  $T_{\perp} / T_{\parallel}$  increases, the shift toward a smaller angle is more strongly dependant on a decrease in  $\beta_{\parallel e}$ , than on a

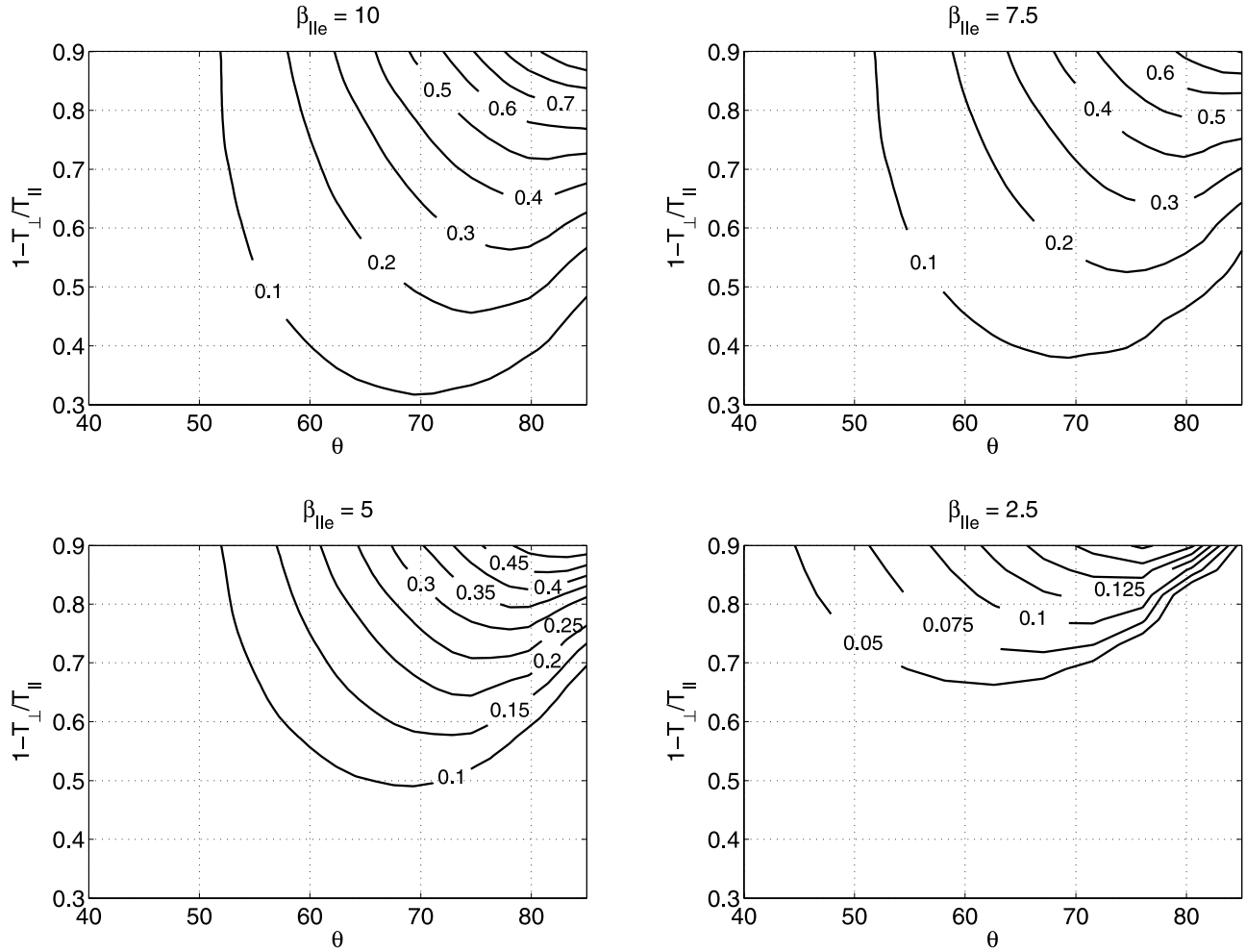


**Figure 1.** Contour plot of the growth rate  $\gamma_m/\Omega_e$  of the nonpropagating EFI as function of the angle  $\theta$  and the anisotropy  $1 - T_{\perp}/T_{\parallel}$  for four different values of  $\beta_{\parallel e} = 10, 7.5, 5,$  and  $2.5$ .

decrease in anisotropy. This is clear if one looks at the four curves for a fixed value of  $T_{\perp}/T_{\parallel}$ : the gap in  $\theta_m$  between the curves becomes more and more enhanced as one moves toward higher values of  $T_{\perp}/T_{\parallel}$ .

[17] It is hence implied from the linear analysis that the evolution of the EFI will concurrently tend to reduce the anisotropy, shift the most unstable modes toward a smaller angle of propagation, and decrease the value of  $\beta_{\parallel e}$  (by the simultaneous effect of the reduction of parallel electron temperature and of the increase of  $|B_0|^2$ ).

[18] Another consequence implied by the linear theory is an “inverse cascade” mechanism [Quest and Shapiro, 1996], namely the transfer of wave power toward smaller wave vectors. Once a linear mode saturates, the decrease in anisotropy excites another linear mode with longer wavelength, thus effectively transferring the power toward smaller wave vectors. This is clearly depicted in Figure 3, where dispersion plots for different values of  $T_{\perp}/T_{\parallel}$  and for four values of  $\beta_{\parallel e}$  are shown. The value of the wave vector  $k_m$  corresponding to the maximum growth rate  $\gamma_m/\Omega_e$  decreases with lower anisotropy, and it is much more influenced by a decrease in anisotropy for fixed  $\beta_{\parallel e}$  than by a decrease in  $\beta_{\parallel e}$  for fixed anisotropy. Also, the range of

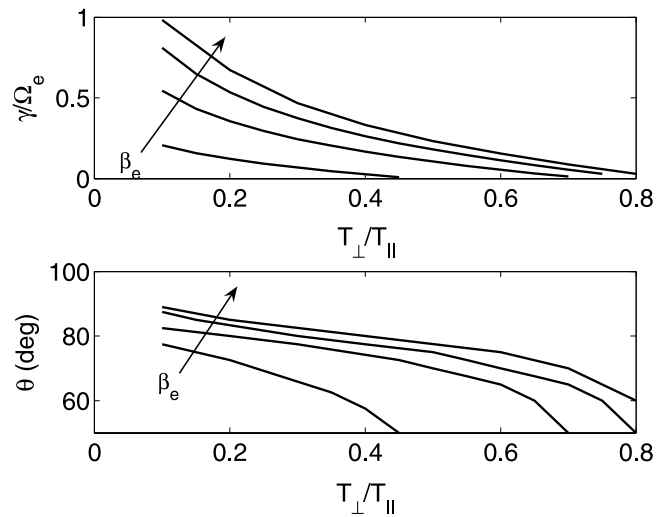


**Figure 2.** Maximum growth rate  $\gamma_m/\Omega_e$  (top) and corresponding angle of propagation  $\theta_m$  (bottom) as functions of  $T_{\perp}/T_{\parallel}$ . The four different curves are for  $\beta_{\parallel e} = 10, 7.5, 5,$  and  $2.5$ , with the arrow indicating increasing direction.

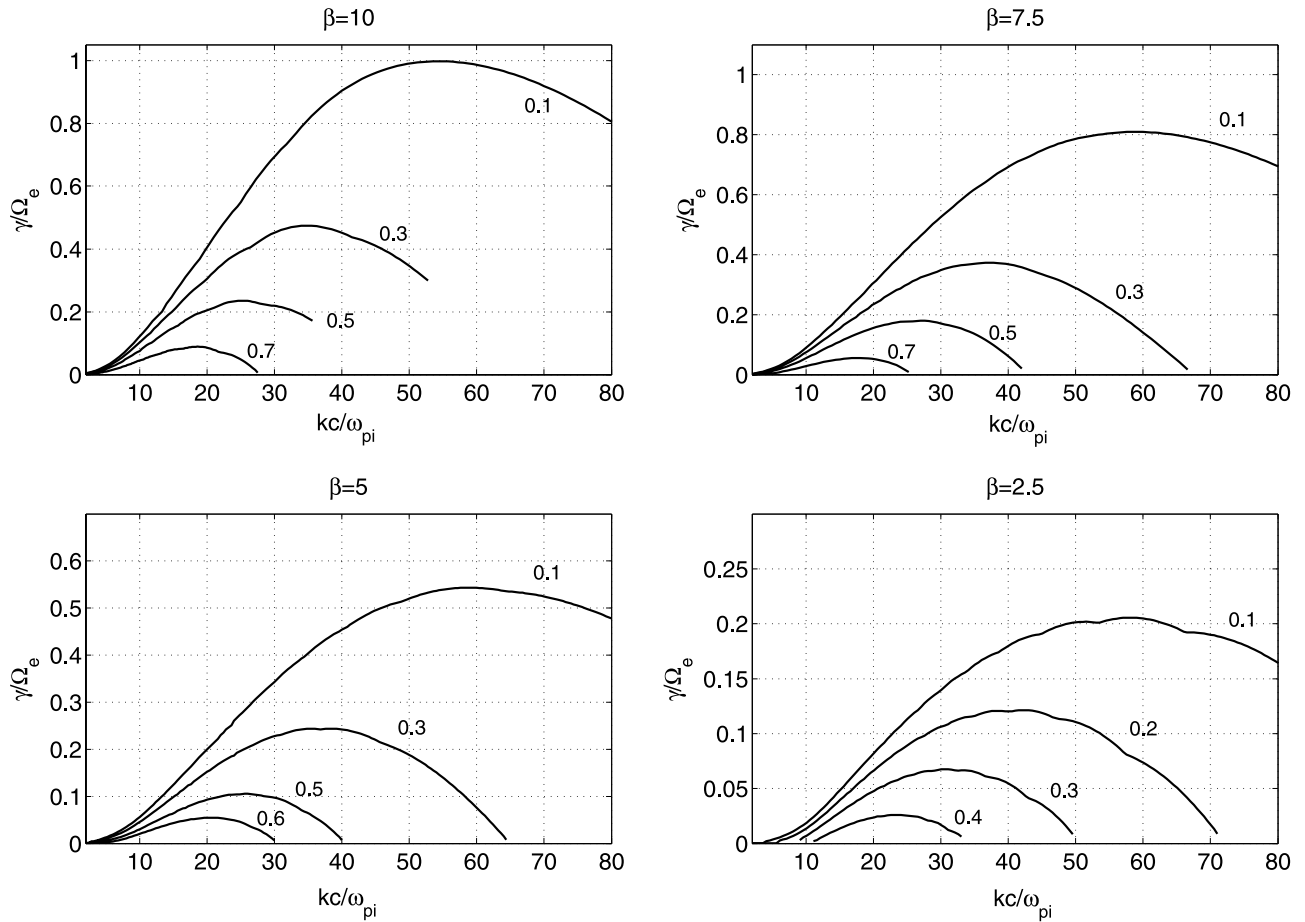


**Figure 3.** Dispersion plots of the maximum growth rate  $\gamma_m/\Omega_e$  for the nonpropagating EFI as functions of  $kc/\omega_{pi}$ . The number on each curve indicates the value of  $T_{\perp}/T_{||}$ . The four panels are for  $\beta_{||e} = 10, 7.5, 5,$  and  $2.5$ .

unstable wave vectors becomes narrower as the anisotropy decreases.

[19] Summarizing, the values of  $\theta_m$  and  $k_m$  both decrease as the instability develops, but while the first has a strong dependence on the value of  $\beta_{||e}$ , the latter is more strongly influenced by the decrease of the anisotropy.

[20] As we mentioned the EFI presents two branches. It has been argued that for the maximum growth rate  $\gamma_m$  the nonpropagating branch is largely dominant. However we show in Figure 4 that, at least for certain angles  $\theta$ , the two branches yield comparable growth rates, and for small enough angles the propagating branch is always dominant. Solid and dashed lines denote, respectively, the nonpropagating and the propagating branches. The left panels in Figure 4 shows  $\gamma_m/\Omega_e$  versus  $\theta$  for three different anisotropies for a fixed value of  $\beta_{||e} = 5$ . The right panel shows the wave vector for the same branches. The  $\omega_r \neq 0$  mode has a slightly longer wave vector for all  $\theta$ . Figure 4 is interesting from the point of view of studying the final stage of the instability, because it shows clearly that propagation at large angles is possible. The appearance of such waves will likely depend on the level of saturation of the fast growing  $\omega_r = 0$  perturbation. If the waves with the highest growth rate saturate soon after the appearance of the

instability, there are reasons to think that propagating waves may be excited. Of course this is only a possible scenario, that will need to be confirmed or refuted by simulations.

[21] Another aspect of the EFI we have investigated is the so-called marginal stability condition, which is a crucial issue in the later discussion. The traditional way to study the marginal stability state is to choose a small value for the growth rate, and to find the appropriate fitting parameters  $S$  and  $\alpha$  such that equation (1) is satisfied for that constant value of  $\gamma$ , within a certain range of  $\beta_{||e}$ . The smallest value for  $\gamma/\Omega_e$  is usually of the order of  $10^{-3}$ . This is because the numerical root-finding algorithm may suffer from inaccuracy or convergence problems for smaller values.

[22] We adopt a slightly different practice, which is more effective and accurate than the commonly used Newton–Raphson method for such small values of  $\gamma$ . We have studied the threshold at  $\gamma = 0$ , within the range  $1 \leq \beta_{||e} \leq 10$ , finding the corresponding value of  $T_{\perp}/T_{||}$  correct up to the third decimal digit, by solving the determinant of  $D$  on a grid  $(\omega_r, \gamma)$  for different values of  $\mathbf{k}$  and  $\theta$ . The value  $\omega$  for which  $|D| = 0$  was then found by numerically calculating the intersections of the curves  $Re(|D|) = 0$  and  $Im(|D|) = 0$ . We also have fitted the solutions into equation (1), and the values for the parameters are:  $S = -1.2951$ ,  $\alpha = 0.9809$ ,

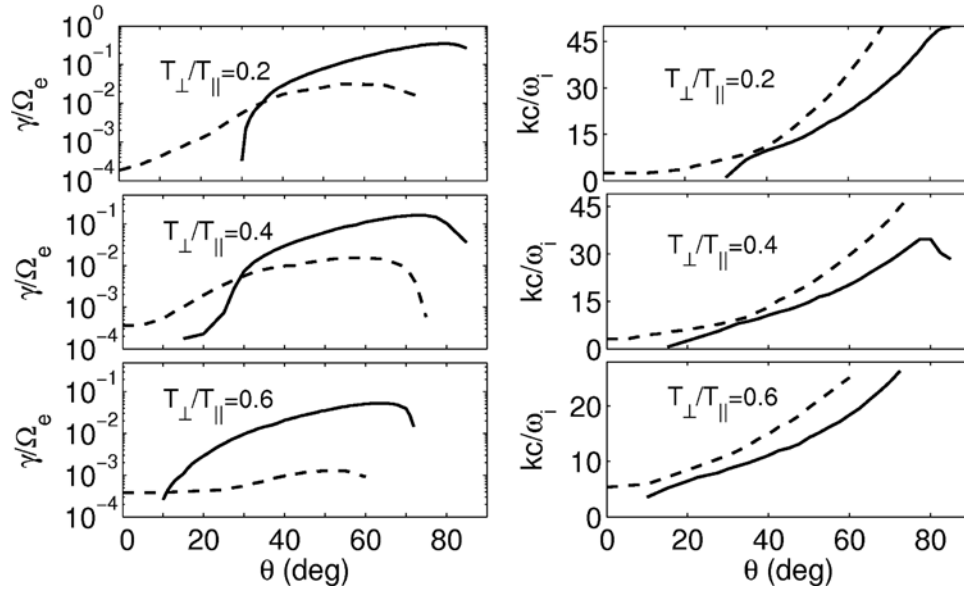


**Figure 4.** Growth rate  $\gamma_m/\Omega_e$  (left) and corresponding wave vector  $kc/\omega_{pe}$  (right) for both propagating (dashed line) and nonpropagating (solid line) EFI modes, as a function of the angle  $\theta$ , for the case  $\beta_{\parallel e} = 5$ .

which are not surprisingly very close to the values found by Gary and Nishimura [2003] for  $\gamma/\Omega_e = 10^{-3}$ .

### 3. Simulations and Results

[23] Here we present the results for simulations run with the two-dimensional version of the parallel implicit PIC code *PARSEK* (for details about the implicit algorithm, see Lapenta *et al.* [2006] and Brackbill and Cohen [1985]). As it is known, the implicit method allows the choice of a timestep  $\Delta t$  and a grid size  $\Delta x$  that do not satisfy the Courant condition  $c\Delta t/\Delta x < 1$  ( $c$  is the speed of light). This condition is instead replaced by a less restrictive constraint, where the speed of light is substituted by the electron thermal velocity, without loss of stability or accuracy [Brackbill and Forslund, 1982].

[24] The computational box ( $x, y$ ) in space is in Cartesian coordinates, and the background magnetic field is along the  $x$ -axis. Particle velocities, electric and magnetic field are all 3D quantities.

[25] We present results of simulations both in one-dimensional and two-dimensional, where the one-dimensional simulation box is aligned with the initially most unstable

wave. The size is chosen so that respectively two and four wavelengths of the most unstable mode fit into the box for two-dimensional and one-dimensional runs. The parameters chosen for all the simulations are given in Table 1, along with the Courant coefficient  $c\Delta t/\Delta x$ , which shows clearly the advantage of using an implicit method. The number of computational particles per cell for each species is 100, and the ion-to-electron mass ratio is physical (i.e.,  $m_i/m_e = 1836$ ).

[26] Every run starts from an unstable region and the instability initially grows from the simulation noise. Figure 5 shows the “trajectory” in the  $(\beta_{\parallel e}, 1 - T_{\perp}/T_{\parallel})$  space of each run as it evolves in time. Superimposed on the same figure is the contour plot of the linear growth rate (the dot-dashed line indicates  $\gamma_m/\Omega_e = 0$ , as derived in the previous section). The growth rate profile for the EFI is qualitatively similar to that for the proton firehose instability (compare with Figure 1 in Matteini *et al.* [2006]). This is a sign that for both instabilities, the isotropic species does not play any particular role in the development of the instability. This is certainly true in our simulations, where the protons do not change their properties and their temperature, remaining Maxwellian. Three aspects of Figure 5 are worthy of

**Table 1.** Parameters of the PIC Simulations<sup>a</sup>

Run #	$\beta_{\parallel e}$	$1 - T_{\perp}/T_{\parallel}$	$L_x\omega_{pe}/c$	$L_y\omega_{pe}/c$	$N_x \times N_y$	$\Delta t\Omega_e$	$\theta_B$ , deg	$c\Delta t/\Delta^b$
1	5	0.5	1.4122	0.514	800 × 400	0.0128	0	5.44
2	5	0.5	0.966	0.0083	760 × 3	0.0110	70	4.72
3	5	0.7	1.3728	0.3678	600 × 300	0.0184	0	8.16
4	5	0.7	0.7106	0.0031	400 × 3	0.0147	80	7.74
5	7.5	0.65	1.9611	0.3458	1200 × 224	0.0128	0	4.53
6	7.5	0.65	0.6811	0.0042	320 × 3	0.0103	80	4
7	10	0.5	0.993	0.0027	520 × 3	0.0064	75	3.88

<sup>a</sup> $L_x$  and  $L_y$  are the length of the box in the  $x$  and  $y$  direction,  $N_x$  and  $N_y$  are the number of cells,  $\Delta t$  is the timestep, and  $\theta_B$  is the angle between the background magnetic field and  $x$ -axis.

<sup>b</sup>Maximum value between  $c\Delta t/\Delta x$  and  $c\Delta t/\Delta y$ .

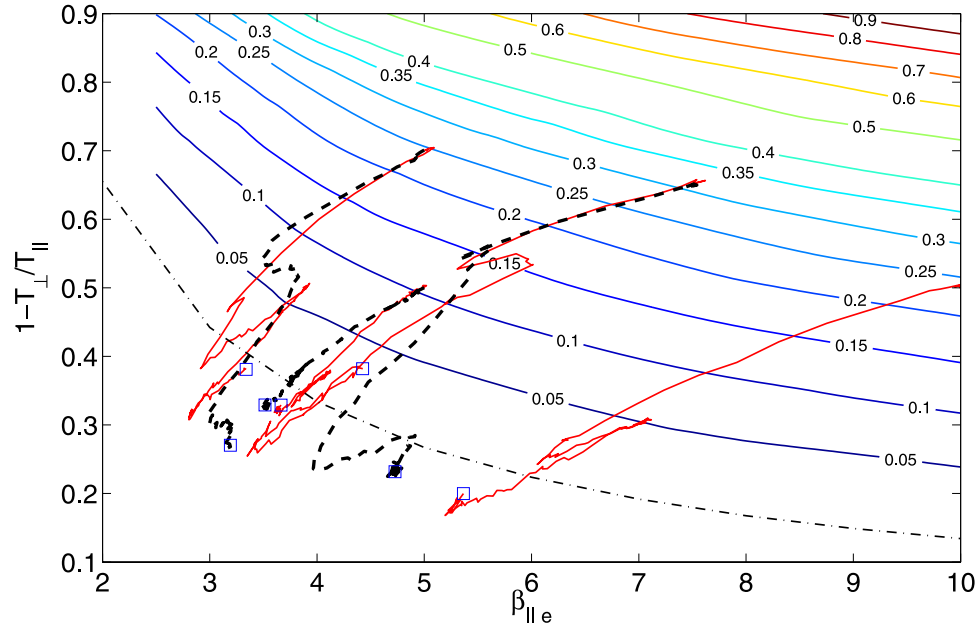


**Figure 5.** The trajectories of the simulations stated in Table 1, plotted in the  $(\beta_{\parallel e}, 1 - T_{\perp}/T_{\parallel})$  space. The contour plot superimposed indicates the linear growth rate  $\gamma_m/\Omega_e$ , and the threshold condition  $\gamma_m/\Omega_e = 0$  is plotted in dot-dashed curves. One-dimensional simulations are plotted in red solid line; two-dimensional simulations are plotted in black dashed line. Squares indicate the end point of a run.

comment. The first is the quantitative difference between the one-dimensional runs (plotted in solid red) and the corresponding two-dimensional runs (plotted in dashed black), that justifies studying the problem in the more complete two-dimensional geometry.

[27] The second aspect is that all the curves at a certain stage approach the marginal stability threshold (plotted as a dot-dashed contour). At that stage for the majority of wave vectors at any angle of propagation, the only linear modes that are solutions of the linear Vlasov equation are damping waves. The effect of quasiperpendicular damped modes on particles and fields is to weaken the magnetic fluctuations, and channel the energy toward particles, predominantly in the parallel direction, thus increasing the anisotropy. Therefore the damping waves and the EFI are two opposite competing mechanisms. The appearance of damping modes in the system while the EFI growth rate is becoming smaller, leads to trajectories that are bouncing around the marginal stability threshold. This happens both for one-dimensional and two-dimensional runs. However, what happens in the case of the slab geometry is that after the initial linear perturbations saturates (and the growth rate becomes small), the damping modes pull back the system to a position where a similar linear perturbation (with the same angle of propagation but smaller wave vector), can grow again, and so on. Hence the pattern of the trajectories is self-similar with stages of growing perturbations (trajectories moving toward bottom left in the  $(\beta_{\parallel e}, 1 - T_{\perp}/T_{\parallel})$  space), followed by damping (trajectories moving top right). Something different happens in the two-dimensional runs. We still have intermittent growing and damping phases, but now the trajectories are not anymore self-similar, in the sense that after the saturation of the most unstable mode, other modes (at different angles) can still grow (and the

trajectories will still move bottom left, but after adjusting onto a different curve).

[28] The third comment is about the low level of anisotropy that all runs can reach. End states are characterized by an anisotropy  $(1 - T_{\perp}/T_{\parallel}) \lesssim 0.3$ . It is probably meaningless to try to attach a certain value of final anisotropy to each run, because that clearly depends on what one considers as the “final value”, due to the oscillations around the threshold experienced by the system. This considerations has strong implications in the definition of the EFI as a constraint for the observed anisotropy in the solar wind. Considering that spacecraft data offer a snapshot of particle properties along a certain period of time, one should not expect to find that electrons have always a level of anisotropy lower than the threshold at  $\gamma = 0$ .

[29] For all the runs the electron distribution function remains approximately bi-Maxwellian and hence is not shown.

[30] We now present and comment in detail on the results from run 5, the others being qualitatively similar. Already from Figure 5 one can notice that the system undergoes several different stages. The linear instability grows rapidly at the beginning, and saturates at  $T\Omega_e \sim 15$ , when the trajectory in Figure 5 adjusts (near the contour  $\gamma/\Omega_e = 0.15$ ) and soon moves toward smaller anisotropy. The development of the magnetic perturbation  $\delta B$  is depicted in the top panel of Figure 6, where the quantity  $|\delta B|^2/|B_0|^2$  is shown in time. The initial linear response is clear. From the time  $T\Omega_e \sim 22$  to time  $T\Omega_e \sim 37$  the perturbation amplitude is very slightly growing, reaching its peak. This corresponds, in Figure 5 to the trajectory rapidly moving from  $\beta_{\parallel e} \sim 5.7$  to  $\beta_{\parallel e} \sim 4$  with correspondingly decreasing anisotropy. From time  $T\Omega_e \sim 37$  onward the amplitude is constantly decreasing (with a local maximum at  $T\Omega_e \sim 72$ , that as we

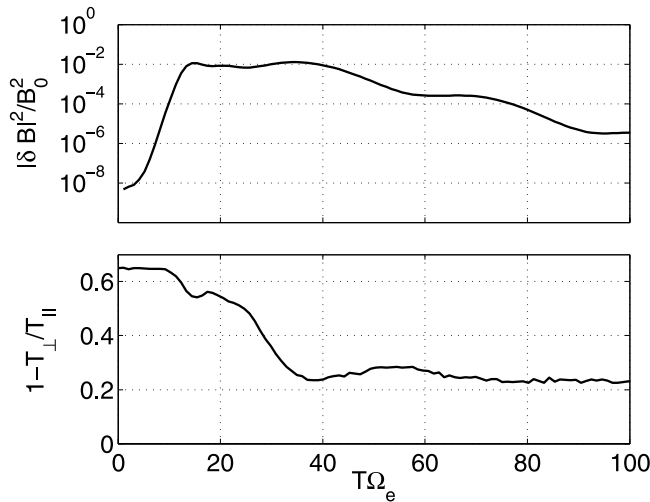


**Figure 6.** Magnetic fluctuation  $|\delta B|^2/B_0^2$  (top) and anisotropy  $1 - T_\perp/T_\parallel$  (bottom) versus time  $T\Omega_e$  for run 5.

will see corresponds to the saturation of a long wavelength mode), and it becomes very low. The bottom panel of Figure 6 shows the developments of the anisotropy. As expected, the anisotropy lowers when the instability grows, and grows during damping phases. It is interesting (and yet another rationale for two-dimensional simulations) that the greater contribution to the decrease of anisotropy (between times  $T\Omega_e \sim 22$  and  $T\Omega_e \sim 37$ ) is not due to the initially most unstable wave (that is indeed already saturated at that time, as we will discuss later). The development of  $\beta_{\parallel e}$  is depicted in Figure 7. The bottom panel shows the factors  $\nabla T_{\parallel e}/|T_{\parallel e}|$  (solid line), and  $|B_0|^2/\nabla B_0^2$  (dashed line), that are the normalized gradients of the numerator and denominator of  $\beta_{\parallel e}$ . Looking at  $\beta_{\parallel e}$ , it follows the same kind of evolution of the anisotropy. What is interesting here is that the increase or decrease of  $\beta_{\parallel e}$  is more controlled by the fluctuations than by the decreasing parallel temperature in the linear stage, and vice versa in the nonlinear stage.

[31] In order to understand the role played by individual modes, and how different waves interact among them, one has to look at the Fourier transform of the magnetic fluctuations. Since the predominant component of the magnetic fluctuations is  $\delta B_z$  (which is the component perpendicular to both  $k$  and  $B_0$ ), we show in Figure 8 the amplitude of the discrete Fourier transform of  $\delta B_z$  for the more dominant wave vectors, as functions of time. For this run the initially most unstable wave is predicted to have  $kc/\omega_{pe} = 36.9$ ,  $\theta = 80^\circ$ . The linear growth of this wave (plotted in blue) is clearly visible, and it is indeed the mode that grows more rapidly. As already mentioned, it saturates at time  $T\Omega_e \sim 15$ . Other quasiperpendicular perturbations grow linearly in this initial stage. In red and green we show waves with  $kc/\omega_{pe} = 18.45$ ,  $\theta = 80^\circ$ , and  $kc/\omega_{pe} = 19.3$ ,  $\theta = 70^\circ$ , respectively. The other three curves represent perturbations with  $\theta = 62^\circ$  (cyan),  $\theta = 54^\circ$  (magenta),  $\theta = 0^\circ$  (black). As predicted, after the breakdown of the linear growth for the most unstable wave, all the other modes continue to grow. Moreover it is interesting that the saturation of the blue curve coincides with a change of slope for the green and red ones. We interpret this feature as the signature that after the

time  $T\Omega_e \sim 15$ , the quasiperpendicular long wavelength modes grow not by a linear mechanism, but by an inverse-cascade mechanism due to the saturation and damping of the most unstable small wavelength mode.

[32] For what concerns the parallel and oblique ( $\theta = 62^\circ$  and  $\theta = 54^\circ$ ) modes, they clearly grow nonlinearly and their amplitude become comparable to the quasiperpendicular modes around the time  $T\Omega_e \sim 55$ . Although it is difficult to identify exactly how the magnetic fluctuation energy is channeled between waves, a certain degree of wave-wave interactions is evident. What is here important, also from an observational point of view, is that the EFI is certainly driven by quasiperpendicular modes in its initial stage, but in the nonlinear stage it supports waves at any angle of propagation. Each of the modes shown is indeed the most dominant over a certain period of time (also the exactly parallel one).

[33] In the previous section we highlighted how the inverse-cascade and the shift toward smaller angle of propagation were implied by the linear theory. The simulations have indeed confirmed that those mechanisms take place, and we now quantify them. We consider the amplitude of the Fourier transform (in space) of all the modes detectable in the computational box. In Figure 9 we present the contour plot of such amplitudes as a function of only  $\theta$  (i.e., integrated over  $k$ ) in the top panel, and as a function of only  $k$  (i.e., integrated over  $\theta$ ) in the bottom panel. Time is on the vertical axis. In the top panel one can see the two peaks at  $\theta = 80^\circ$  and  $\theta = 70^\circ$  that just confirm the discussed growth of the blue and red lines in Figure 8. However it is probably more interesting to note what happens from time  $T\Omega_e = 50$  onward. The energy becomes rapidly distributed over a broad range of angles (from  $\theta \sim 30^\circ$  to  $\theta \sim 80^\circ$ ), and the quasiperpendicular propagation is not anymore dominant. As for the inverse-cascade mechanism, the bottom panel shows that the energy moves from being centered around  $kc/\omega_{pe} = 36.9$  to  $kc/\omega_{pe} \sim 20$ . In this case however the inverse-cascade does not proceed further at longer times.

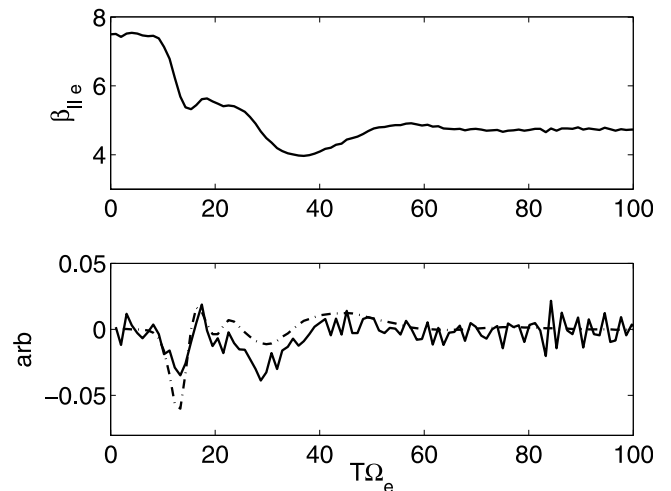


**Figure 7.** (top)  $\beta_{\parallel e}$  versus time  $T\Omega_e$ . (bottom) Factors  $\nabla T_{\parallel e}/|T_{\parallel e}|$  (solid line) and  $|B_0|^2/\nabla B_0^2$  (dashed line), which are the normalized gradients of the numerator and the denominator of  $\beta_{\parallel e}$ , versus time. Both panels are for run 5.

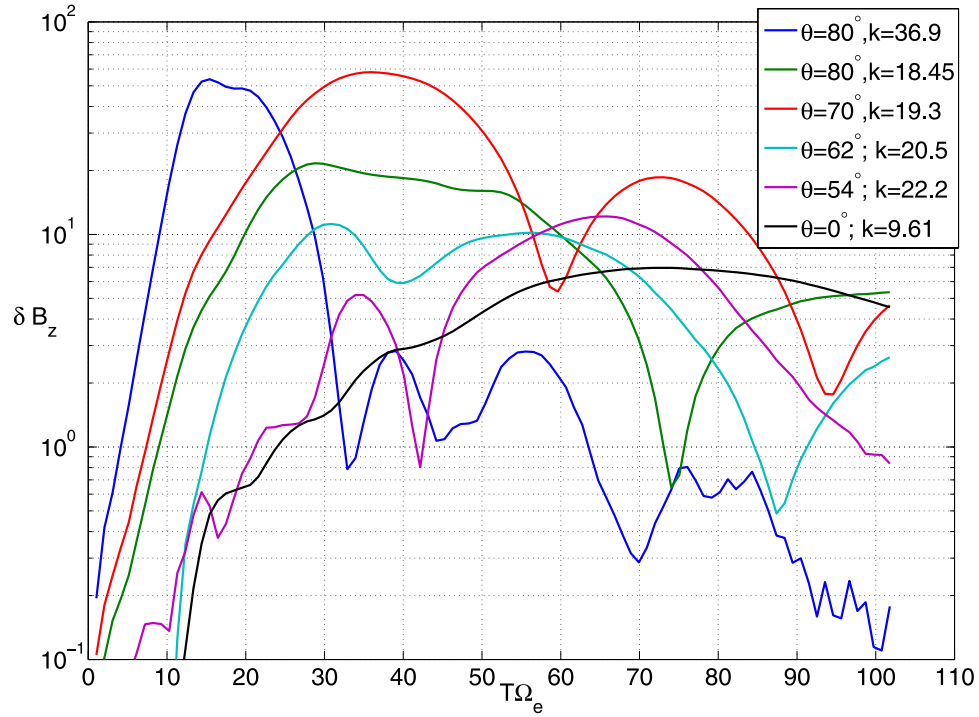


**Figure 8.** Amplitude of the Fourier transform of  $\delta B_z$  versus time  $T\Omega_e$  for the predominant mode in the simulation. The wave vector  $k$  in the legend is intended normalized with respect to  $c/\omega_{pi}$ .

[34] To conclude our analysis we show in Figure 10 the Fourier transform in time of some of the modes we already discussed in Figure 8. The period over which the transform is performed is from  $T\Omega_e = 37$  to the end of the simulation.

We are interested in detecting any linear mode that can be identified as the remnant of the EFI process. In order to do so we have solved the linear Vlasov problem, for  $\beta_{\parallel e} = 4.7$ , and  $T_{\perp}/T_{\parallel} = 0.77$  (the average parameter values for this

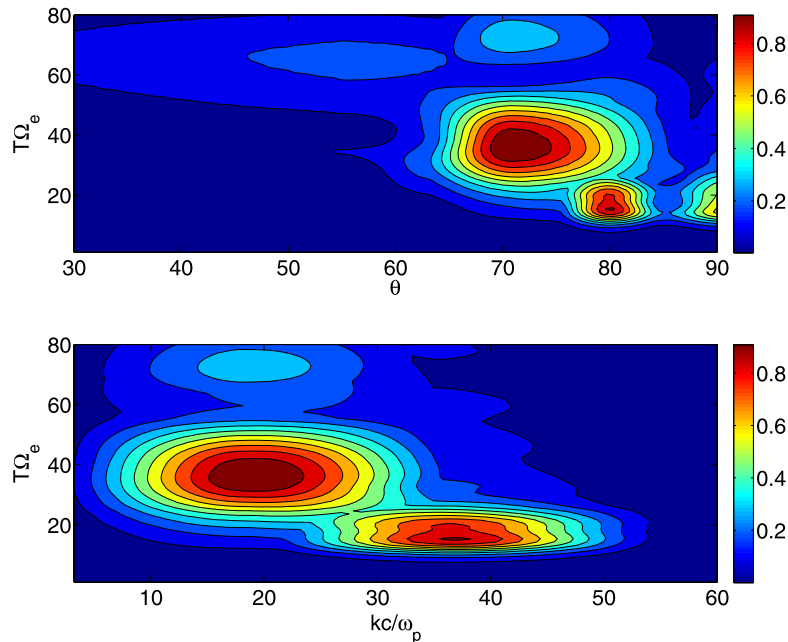


**Figure 9.** Contour plot of the amplitude of the Fourier transform of  $\delta B_z$  versus time (on vertical axes) as a function of the angle  $\theta$  (top) and of the wave vector  $kc/\omega_{pi}$  (bottom).

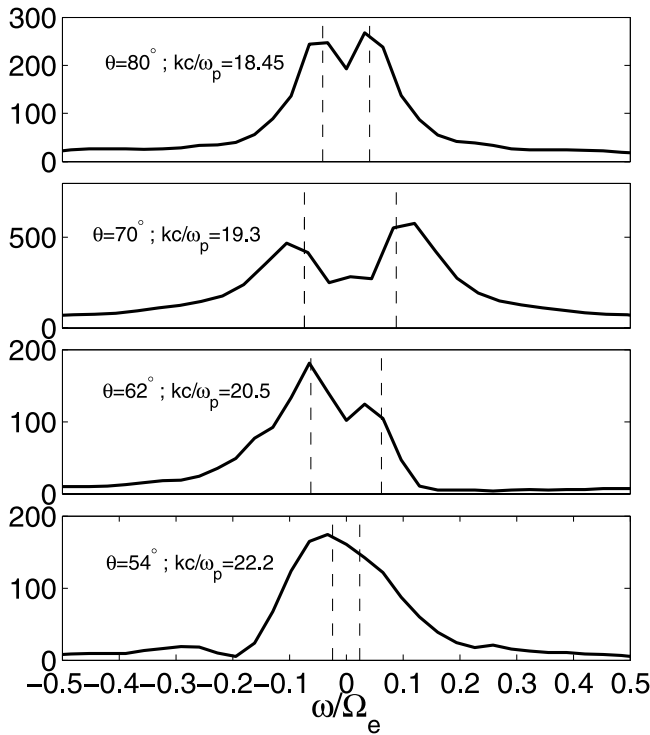


**Figure 10.** Fourier transform in time for four different modes ( $\theta$  and  $kc/\omega_{pi}$  stated in the panels). The dashed lines are the real frequency of a linear Vlasov solution for average parameters  $\beta_{\parallel e} = 4.7$  and  $T_{\perp}/T_{\parallel} = 0.77$ .

period), for those four wave vectors. The system yields only damping modes, being below the marginal stability threshold, and the real frequency of one of the solutions is plotted in Figure 10 as a vertical dashed line. As one can see the peaks of the Fourier transform and this linear mode are very close, thus indicating that one can indeed describe the final stage of the simulation in terms of damping linear modes. The linear solution that we have found to be closest to the peaks of the Fourier transform is the extension of the oblique whistler/electron–cyclotron mode to short wavelengths (using the terminology adopted in Gary [1993, p. 113]). However we need to point out that slower modes would not be detectable in our Fourier analysis, since the simulations are not run for long enough.

[35] It is an interesting question whether the EFI, after it has operated and brought the electron distribution toward marginal stability, leaves any observational signature. So for the same four modes, we have computed the Doppler-shifted frequency  $\omega = \omega_r - \mathbf{k} \cdot \mathbf{V}_{SW}$ , that would be the frequency observed by a spacecraft embedded in a wind with speed  $\mathbf{V}_{SW}$ . We have chosen an hypothetical solar wind with velocity 500 km/s, and electron cyclotron frequency equal to 1214 Hz. The Doppler-shifted frequency is of course a function of the angles  $\theta_{SW}$  between the solar wind velocity and  $B_0$ , and  $\theta_B$  between  $\mathbf{k}$  and  $B_0$ . For a fixed  $\theta_{SW}$ , its maximum and minimum are found for the case in which  $\mathbf{k}$ ,  $\mathbf{V}_{SW}$ , and  $B_0$  are coplanar, and are expressed as  $\omega = \omega_r - k \times V_{SW} \cos(\theta_B \pm \theta_{SW})$ . This quantity is plotted (in Hz) in Figure 11 as a function of  $\theta_{SW}$  for the four different modes ( $\theta$  and  $k$  are reported in caption). Although

this figure is not intended to represent the large range of parameters in which the solar wind can be found, it gives a qualitative idea of the low frequency range in which one should expect to find these modes. The orientation of the wave perturbation is predominantly along  $\delta B_z$ , i.e., perpendicular to both  $\mathbf{k}$  and  $B_0$ .

#### 4. Conclusions

[36] The electron kinetic firehose instability is driven by an electron parallel temperature greater than the perpendicular one, and it is thought to be an important process in some astrophysical contexts (e.g. the solar wind) to determine the upper bound of the electron anisotropy. We have studied the EFI via linear theory and PIC simulations. Although it is well known that the solar wind presents nonthermal features in its particle distribution function, we have assumed a bi-Maxwellian electron population, so the present study is relevant only to the core part of the distribution.

[37] The linear analysis predicts that as the instability develops two phenomena will occur: the inverse-cascade of fluctuation energy toward longer wavelengths, and the shift of the most unstable modes toward smaller angles of propagation. Moreover, we have shown that the propagating branch of the instability can extend to quasiperpendicular directions, and although the instability is initially driven by nonpropagating modes, we have conjectured that oblique propagating perturbations could develop in the nonlinear stage of the process.

[38] This suggests that fully nonlinear PIC simulations, in a two-dimensional geometry, are needed in order to comprehend most of the physical processes that take place.

[39] We have shown the results for several runs in one-dimensional and two-dimensional geometry. The development of the EFI proceeds as follows. The linear growth of

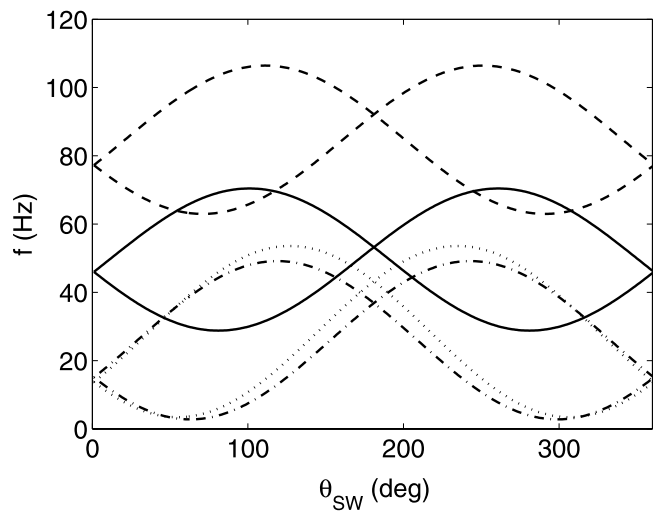


**Figure 11.** Doppler-shifted frequency range (see text for definition) of the same four modes plotted in Figure 10:  $\theta = 80^\circ$ ,  $kc/\omega_{pi} = 18.45$  (solid);  $\theta = 70^\circ$ ,  $kc/\omega_{pi} = 19.3$  (dashed);  $\theta = 62^\circ$ ,  $kc/\omega_{pi} = 20.5$  (dotted);  $\theta = 54^\circ$ ,  $kc/\omega_{pi} = 22.2$  (dash-dotted). The frequencies are in Hz, and the electron cyclotron frequency is 1214 Hz.

the instability is driven by quasiperpendicular modes, and the anisotropy is rapidly reduced. Those modes soon saturate and damp. Wave–wave interactions take place and the fluctuation energy moves toward smaller and less oblique wave vectors. As the system approaches its marginal stability threshold, linear damping modes start to play a major role in the process. In the final stage the linear instability and the damping modes compete to move the system respectively toward smaller and larger values of anisotropy and electron parallel beta. This means that the end state of the plasma is effectively bouncing around the marginal stability threshold, and therefore one should not expect to never observe particle distribution functions above the threshold, in order to state that the EFI is effectively acting as a constraint on the electron anisotropy.

[40] From an observational point of view there are two important remarks that need to be emphasized. Although the instability is initially driven by quasiperpendicular, non-propagating modes, in the nonlinear stage a high level of fluctuations can be detected at any angle of propagation. Also, in the final stage, the damping modes can give rise to propagating waves, that we have interpreted as the extension to short wavelengths of the oblique whistler/electron–cyclotron mode. Those are low frequency modes and we have predicted their Doppler-shifted frequency in a hypothetical 500 km/s solar wind, with  $\Omega_e = 1214$  Hz, to be  $\lesssim 100$  Hz. This is an important signature that the firehose instability has operated, and we propose it as observational evidence (although probably not easy to detect) in favor of the ongoing debate about the role of the EFI and the thermal properties of the observed electron distribution function in the solar wind.

[41] **Acknowledgments.** We would like to thank Prof. Giovanni Lapenta and Stefano Markidis for their assistance with the code *PARSEK*. E. Camporeale is funded by a studentship from Queen Mary, University of London.

[42] Amitava Bhattacharjee thanks Lorenzo Matteini and Wendell Horton for their assistance in evaluating this paper.

## References

- Brackbill, J. U., and B. I. Cohen (1985), *Multiple Time Scales*, Academic Press, Orlando, Florida.
- Brackbill, J. U., and D. W. Forslund (1982), An implicit method for electromagnetic plasma simulation in two dimensions, *J. Comput. Phys.*, *46*, 271–308.
- Chew, G. F., M. L. Goldberger, and F. E. Low (1956), The Boltzmann equation and the one-fluid hydromagnetic equations in the absence of particle collisions, *Proc. R. Soc. London, Ser. A*, *236*, 112.
- Gary, S. P. (1993), *Theory of Space Plasma Microinstabilities*, p. 193, Cambridge Univ. Press, Cambridge, UK, September.
- Gary, S. P., and C. D. Madland (1985), Electromagnetic electron temperature anisotropy instabilities, *J. Geophys. Res.*, *90*, 7607–7610.
- Gary, S. P., and K. Nishimura (2003), Resonant electron firehose instability: Particle-in-cell simulations, *Phys. Plasmas*, *10*(9), 3571–3576.
- Gary, S. P., D. Winske, and M. Hesse (2000), Electron temperature anisotropy instabilities: Computer simulations, *J. Geophys. Res.*, *105*, 10,751–10,760.
- Gary, S. P., B. Lavraud, M. F. Thomsen, B. Lefebvre, and S. J. Schwartz (2005), Electron anisotropy constraint in the magnetosheath: Cluster observations, *Geophys. Res. Lett.*, *32*, L13109, doi:10.1029/2005GL023234.
- Hellinger, P., P. Trávníček, J. C. Kasper, and A. J. Lazarus (2006), Solar wind proton temperature anisotropy: Linear theory and WIND/SWE observations, *Geophys. Res. Lett.*, *33*, L09101, doi:10.1029/2006GL025925.
- Kasper, J. C., A. J. Lazarus, and S. P. Gary (2002), Wind/SWE observations of firehose constraint on solar wind proton temperature anisotropy, *Geophys. Res. Lett.*, *29*(17), 1839, doi:10.1029/2002GL015128.
- Lapenta, G., J. U. Brackbill, and P. Ricci (2006), Kinetic approach to microscopic-macroscopic coupling in space and laboratory plasmas, *Phys. Plasmas*, *13*, 5904+, doi:10.1063/1.2173623.
- Li, X., and S. R. Habbal (2000), Electron kinetic firehose instability, *J. Geophys. Res.*, *105*, 27,377–27,386.
- Matteini, L., S. Landi, P. Hellinger, and M. Velli (2006), Parallel proton fire hose instability in the expanding solar wind: Hybrid simulations, *J. Geophys. Res.*, *111*, A10101, doi:10.1029/2006JA011667.
- Matteini, L., S. Landi, P. Hellinger, F. Pantellini, M. Maksimovic, M. Velli, B. E. Goldstein, and E. Marsch (2007), Evolution of the solar wind proton temperature anisotropy from 0.3 to 2.5 AU, *Geophys. Res. Lett.*, *34*, L20105, doi:10.1029/2007GL030920.
- Messmer, P. (2002), Temperature isotropization in solar flare plasmas due to the electron firehose instability, *Astron. Astrophys.*, *382*, 301–311, doi:10.1051/0004-6361:20011583.
- Paesold, G., and A. O. Benz (1999), Electron firehose instability and acceleration of electrons in solar flares, *Astron. Astrophys.*, *351*, 741–746.
- Paesold, G., and A. O. Benz (2003), Test particle simulation of the electron firehose instability, *Astron. Astrophys.*, *401*, 711–720, doi:10.1051/0004-6361:20030113.
- Quest, K. B., and V. D. Shapiro (1996), Evolution of the fire-hose instability: Linear theory and wave-wave coupling, *J. Geophys. Res.*, *101*, 24,457–24,470.
- Stix, T. H. (1992), *Waves in Plasmas*, American Institute of Physics, New York.
- Stverak, S., P. Trávníček, E. Maksimovic, E. Marsch, A. N. Fazakerley, and E. E. Scime (2008), Electron temperature anisotropy constraints in the solar wind, *J. Geophys. Res.*, *113*, A03103, doi:10.1029/2007JA012733.

E. Camporeale and D. Burgess, Astronomy Unit, Queen Mary University of London, Mile End Road, London E1 4NS, UK. (e.camporeale@qmul.ac.uk; d.burgess@qmul.ac.uk)